Directionality of metal-induced crystallization and layer exchange in amorphous carbon/nickel thin film stacks

Janke, D.; Munnik, F.; Julin, J. A.; Hübner, R.; Grenzer, J.; Wüstefeld, C.; Gemming, S.; Rafaja, D.; Krause, M.;

Originally published:

December 2020

Carbon 159(2020), 656-667

DOI: https://doi.org/10.1016/j.carbon.2019.12.006

Journal Pre-proof

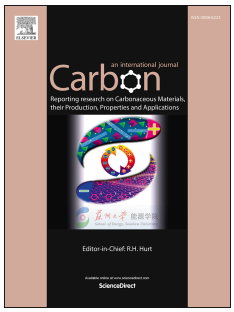

Directionality of metal-induced crystallization and layer exchange in amorphous carbon/nickel thin film stacks

Daniel Janke, Frans Munnik, Jaakko Julin, René Hübner, Jörg Grenzer, Christina Wüstefeld, Sibylle Gemming, David Rafaja, Matthias Krause

PII: S0008-6223(19)31238-2

DOI: https://doi.org/10.1016/j.carbon.2019.12.006

Reference: CARBON 14856

To appear in: *Carbon*

Received Date: 26 September 2019

Revised Date: 24 November 2019

Accepted Date: 4 December 2019

Please cite this article as: D. Janke, F. Munnik, J. Julin, René. Hübner, Jö. Grenzer, C. Wüstefeld, S. Gemming, D. Rafaja, M. Krause, Directionality of metal-induced crystallization and layer exchange in amorphous carbon/nickel thin film stacks, *Carbon* (2020), doi: https://doi.org/10.1016/j.carbon.2019.12.006.

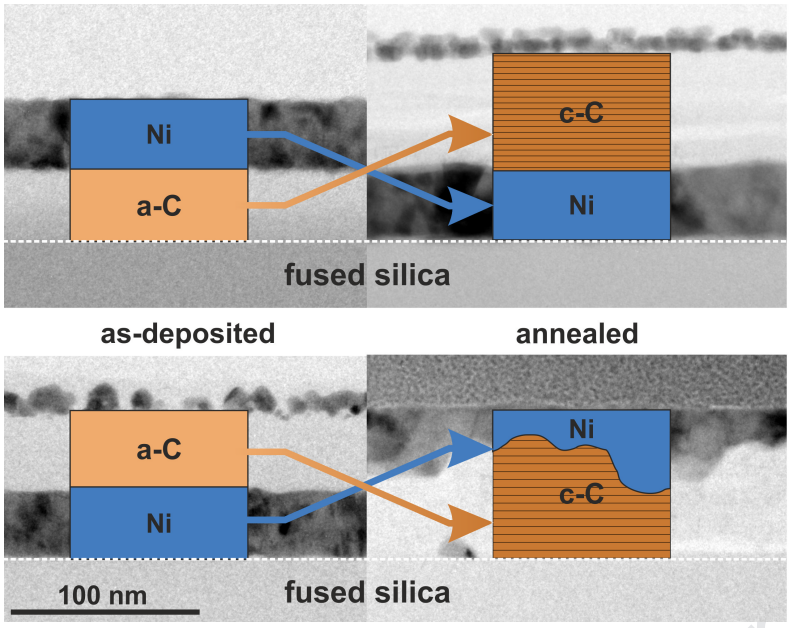

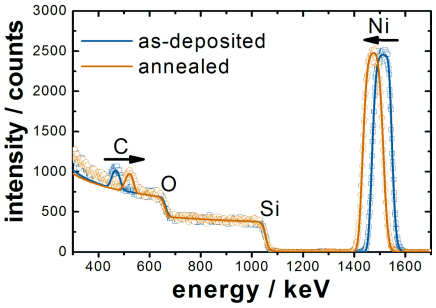

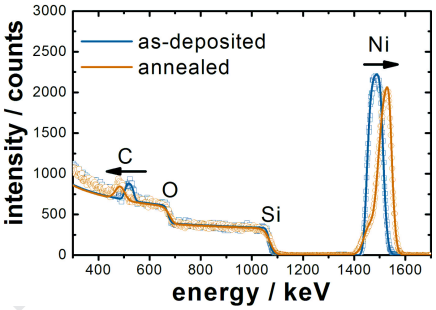

Directionality of metal-induced crystallization and layer exchange in amorphous carbon/nickel thin film stacks

Daniel Janke[a], Frans Munnik[a], Jaakko Julin[a], René Hübner[a], Jörg Grenzer[a], Christina Wüstefeld[b], Sibylle Gemming[a,c], David Rafaja[b], Matthias Krause[a*]

[a] Helmholtz-Zentrum Dresden – Rossendorf, Bautzner Landstraße 400, 01328 Dresden, Germany

[b] Institute of Materials Science, TU Bergakademie Freiberg, Gustav-Zeuner-Straße 5, 09599 Freiberg, Germany

[c] Institute of Physics, TU Chemnitz, Reichenhainer Straße 70, 09126 Chemnitz, Germany

Abstract

In thin amorphous carbon (a-C) films being in contact with a thin nickel layer, metal-induced crystallization and layer exchange (LE) occur at temperatures lower than 700 °C. Analysis of thin film stacks with different architectures (a-C/Ni, Ni/a-C and Ni/a-C/Ni) by means of ion beam analysis, Raman spectroscopy, X-ray diffraction and transmission electron microscopy revealed that the degree of LE and the structural quality of the crystallized carbon layers depend on the initial layer sequence. A LE degree of approx. 93 % was found for a-C/Ni bilayers, where graphenic layers formed on the Ni surface, whereas in Ni/a-C bilayers only 83 % of carbon was transferred from the surface towards the fused silica substrate. The diffusion of carbon in the outward direction produces turbostratic carbon with basal planes oriented parallel to the Ni surface, while for the inward direction planar and curved turbostratic structures coexist. The crystallization and the LE are driven by the crystallization energy of a-C. The LE is mediated by the wetting of the Ni grain boundaries by carbon. The directionality of the LE was explained primarily by the difference in the surface and interface energies in the a-C/Ni and Ni/a-C stacks that were obtained from thermodynamic considerations.

[*] Corresponding author. Tel.: +493512603578; e-mail: matthias.krause@hzdr.de

1. Introduction

A complete transformation of amorphous carbon (a-C) into graphite requires temperatures of approximately 3000 °C and proceeds via various intermediate states of graphenic carbon that form between 1000 and 3000 °C.[1-5] These temperatures restrict the usable substrate materials for thermally-induced crystallization of a-C thin films immensely. However, bringing the a-C layers in contact with suitable catalysts lowers the crystallization temperature significantly. The underlying reaction type was termed catalytic graphitization.[3,6] It can proceed via the mechanisms of carbon dissolution-precipitation[7-9], metal-mediated or metal-induced crystallization (MMC and MIC)[10,11] and metal-enhanced surface diffusion[12,13]. Carbon crystallization based on dissolution-precipitation occurs on both sides of a catalyst thin film. In the case of enhanced diffusion, the carbon crystallizes at the carbon source exposed surface. In the MIC process, the carbon crystallization can be accompanied by an exchange of the metal and carbon layers. The dominant mechanism depends strongly on the nature of the metal catalyst, applied temperature, amount of catalyst and carbon, and on the use of diffusion barriers[14]. Hence, the identification and explanation of the dominant mechanisms of both processes require depth-resolved information about the chemical composition and the detailed structure analysis of the layers.

First experiments on MIC of a-C were carried out by Sinclair and Konno with carbon-cobalt thin films.[10] Many further studies were done on nickel-carbon thin film layer stacks, because nickel is one of the most powerful catalysts for carbon crystallization[6,15] due to the small mismatch (≈ 1 %) between (111)-oriented Ni lattice planes and basal planes of graphite, favourable p_π-d_π-interaction, thermodynamic instability of Ni carbides[16] and a low solubility of carbon in nickel[17]. Using differential scanning calorimetry, Sinclair et al. found a temperature of 540 °C for the crystallization of a-C in a-C/Ni/a-C trilayers.[18] This value for the crystallization temperature was recently confirmed by other groups[14,19-21]. In order to improve the structural order of the obtained graphene layers, diffusion barriers of Al_2O_3 or SiO_2 were deposited between the Ni and a-C layers[14,19]. In an *in situ* X-ray study, a crystallization temperature between 640 °C and 730 °C was reported, which is significantly higher than in the majority of

studies.[22] These studies on MIC of a-C in a-C/Ni thin film stacks focussed mainly on the synthesis of high-quality few-layer graphene by a competing method to CVD and on the increase of the lateral crystallite size of the crystallized carbon (c-C). They address either the outward or the inward crystallization.

So far, no study exists on the directionality of the MIC accompanied by a layer exchange (LE) process in a-C/metal thin film stacks. A comparative, quantitative investigation of the LE degree as a function of the initial stacking order and a corresponding systematic microstructure characterization of the stacks before and after LE and MIC are lacking. Still, these tasks are crucial for understanding the underlying mechanisms and driving forces, and consequently for application of these mechanisms for the production of thin graphenic slabs with controlled microstructure. As a first step in this direction, the degree of LE has recently been introduced in order to quantify the degree of LE for Ni/a-C thin film stacks.[23]

In the current paper, the directionality of MIC with LE in a-C/Ni thin film stacks is studied by quantitative elemental depth profiling and microstructure analysis. The directionality of LE is substantiated by applying thermodynamic estimations for the energetic contributions to the overall free energy of the outward and inward direction of carbon crystallization. The structures after the layer exchange are termed turbostratic carbon, their basal planes are termed graphenic planes and the transformation process of amorphous into turbostratic carbon is termed (metal-induced) crystallization.[24]

2. Experimental methods

2.1. Film growth and annealing

For this study, a-C/Ni and Ni/a-C bilayer stacks and a Ni/a-C/Ni trilayer stack were deposited at room temperature (RT) on fused silica (SiO_2) substrates by high power impulse magnetron sputtering (HiPIMS).[25] The Ni and C targets with the purity of 99.99 % and 99.95 % were mounted in a bottom-up dual-beam geometry and operated at magnetron powers of 200 W and 300 W, respectively. In order to exclude cross-contamination, the inactive target was covered by a shutter. Sequential deposition without breaking the vacuum prevented the oxidation of the

Ni/a-C interface. The Ni and C layers were deposited with thicknesses of 40 ± 10 nm.[a] For TEM imaging, the bilayer stacks were deposited on thermally oxidized, (100)-oriented Si wafers.

The stack notations throughout this work refer to the initial state. Ni/a-C is used for Ni deposited on a-C for the LE in the outward direction, where the carbon atoms diffuse towards the sample surface. a-C/Ni denotes a-C deposited on Ni for the LE in the inward direction. In this case, the carbon atoms diffuse towards the substrate.

The MIC was activated by annealing the samples in high vacuum (10^{-7} – 10^{-5} Pa). The samples were heated from the substrate side. The heating rate was set to 6 K min^{-1} between RT and 100 °C and to 30 K min^{-1} in the range 100 – 700 °C. After a dwell time of 1 hour at 700 °C, the samples were cooled to RT with a rate of 30 K min^{-1}.

2.2. Characterization

The depth-resolved chemical composition of the samples was determined using Rutherford backscattering spectrometry (RBS) and elastic recoil detection analysis (ERDA), both before and after annealing. The ion beam analysis was performed employing the 6 MV tandem accelerator of the Ion Beam Center at HZDR[26]. For RBS, 2 MeV He^{+} ions were focused on a 1×1 mm^2 beam spot on the sample surface. The backscattered ions were detected using a silicon surface-barrier detector covered by a 100 nm Al layer under a scattering angle of 165°[27]. SIMNRA software[28] was employed to obtain the layer composition, areal density and interface roughness. ERDA was applied as a complementary technique to achieve a higher accuracy and lower detection limit for carbon and oxygen. For the recoil ejection, 43 MeV Cl^{7+} ions were used. The Cl ions were focused on a 1×1 mm^2 beam spot and detected under a scattering angle of 31° by means of a Bragg ionisation chamber that uses a full energy detection circuit for the ion energies and a fast timing circuit to obtain a Z-dependent signal to separate the individual ions. The spectra of the recoiled species and the scattered Cl ions were fitted simultaneously using the program NDF v9.3gi[29], which reveals finally the concentration depth profiles.

[a] Additional investigations were performed on layers with the thickness between 10 and 100 nm, thus the presented results are valid in this broader range.

The carbon layers were characterized using micro-Raman spectroscopy and transmission electron microscopy with high resolution (HRTEM). The experimental setup used for the micro-Raman measurements comprised a fibre-coupled diode-pumped solid-state laser emitting a primary beam with the wavelength of 532 nm and a Horiba iHR 550 spectrograph. The laser power on the sample was 1 mW, and the laser spot diameter was 5 µm. The Raman scattered light was dispersed by a holographic 1800 mm^{-1} grating and detected by a liquid nitrogen cooled, back-illuminated deep-depleted Si CCD array.[27] The Raman spectra were fitted as described by Wenisch et al.[13] The denomination of the spectral lines corresponds to the nomenclature suggested by Ferrari at al.[30] The cross-sectional TEM investigations were performed using an image C_s corrected Titan 80 - 300 microscope (FEI) operated at an accelerating voltage of 300 kV. TEM specimens were prepared using a "classical" procedure including sawing (Wire Saw WS 22, IBS GmbH), grinding (MetaServ 250, Bühler), polishing (Minimet 1000, Bühler), dimpling (Dimple Grinder 656, Gatan), and final Ar+ ion milling (Precision Ion Polishing System PIPS 691, Gatan).[31]

The residual stresses, stress-free lattice parameters and crystallite sizes in the Ni layers were deduced from the X-ray diffraction measurements that were performed in glancing-angle diffraction geometry (GAXRD) on an Empyrean diffractometer (PANalytical). The diffractometer was equipped with a copper anode ($\lambda_{Cu\text{-}K\alpha}$), parabolic Goebel mirror producing parallel primary X-ray beam and parallel plate collimator having the opening of 0.27°. The angle of incidence of the primary beam was set to 1° in order to reduce the penetration depth of the X-rays into the volume of the sample. The XRD patterns were measured in the range of 10 – 100° 2θ in steps of 0.05°.

3. Results

3.1. Proof of the layer exchange

Figure 1 displays the RBS spectra of both bilayer stacks in the as-deposited state and after annealing. The spectra before annealing (blue lines) show symmetric Ni and C peaks. In order to determine the concentrations of the species, RBS spectra (Fig. 1) were fitted using a multi-

layer sample model.[28] The simulations revealed the areal densities of Ni and C of 590×10^{15} and 690×10^{15} at. cm^{-2} (480×10^{15} and 690×10^{15} at. cm^{-2}) for the initial Ni/a-C (a-C/Ni) stack. Before annealing, the Ni and C layers consisted of single elements, apart from a small amount of Ar ($< 5\times10^{15}$ at. cm^{-2}) incorporated into both layer stacks during the deposition.

In the annealed Ni/a-C layer stack, the centre of gravity of the Ni signal had shifted from $E_{RBS} \approx 1520$ keV to lower backscattering energies ($E_{RBS} \approx 1480$ keV), cf. Fig. 1a. In contrast, the C signal, whose centre was initially located at $E_{RBS} \approx 470$ keV, shifted to higher backscattering energies ($E_{RBS} \approx 520$ keV). Thus, after annealing an inverse stacking order of Ni and C was found. For the a-C/Ni layer stack, the RBS peaks shifted by approximately the same energy difference but in the inverted directions (see Fig 1b). In both annealed stacks, the Ar signal is broader than in the as-deposited ones, and is nearly indistinguishable from the background noise. In the SIMNRA simulation[28] of the annealed stacks, the a-C/Ni (Ni/a-C) layers were described as Ni and C triple-layer structure with minor fractions of the respective other element.

Although both layer stacks (a-C/Ni and Ni/a-C) experienced the same thermal treatment, the layer exchange shows a distinct directionality that becomes evident from the comparison of the Ni peak shapes. While the Ni peak remains symmetric after the outward LE, it becomes clearly asymmetric after the inward LE. A low-energetic shoulder, which corresponds to the Ni areal density of approx. 75×10^{15} at. cm^{-2}, is found at the original position of the Ni peak (Fig. 1b). This means that a minor fraction of Ni did not undergo the layer exchange, but is still located at the substrate like in the initial sample. The LE directionality is also revealed by the C signals. In contrast to the outward LE direction, where solely the shift of the C peak was observed, the C peak shift observed after inward LE is accompanied by peak broadening and by the drop of the peak amplitude. These effects indicate that in the annealed a-C/Ni stack a minor fraction of C atoms might be located inside the Ni layer.

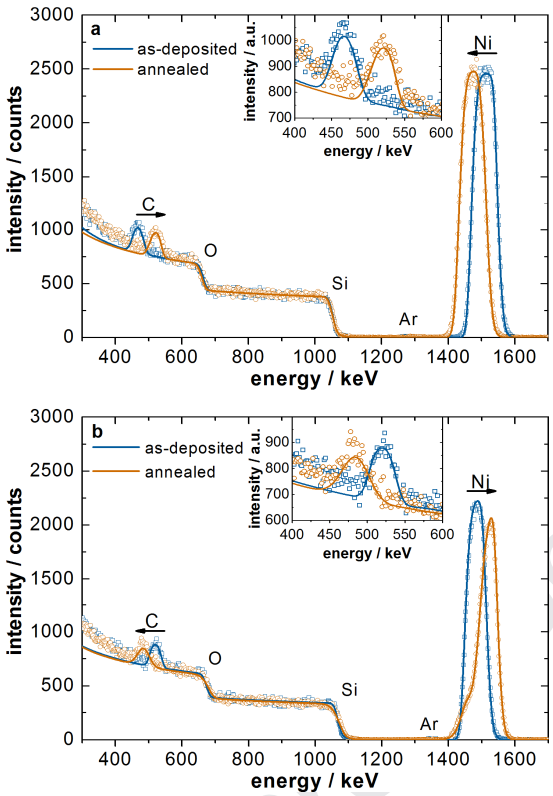

Figure 1: RBS spectra of the as-deposited and annealed Ni/a-C (a) and a-C/Ni (b) layer stacks. Solid lines represent SIMNRA[27] simulations. The insets show the magnified carbon signal. The difference between the measured and simulated intensities at low energies (< 400 keV) is caused by multiple scattering, which is not reproduced correctly in the simulation.

The substrate elements Si and O give rise to broad plateaus, whose edges are found at the same position for both stacking orders and for both LE directions. This indicates that incoming He^+ ions experienced the same degree of stopping within both layer stacks, which means that the total areal densities of C and Ni should be conserved. This was confirmed by the comparison of the layer areal densities of the annealed samples obtained from the SIMNRA simulation of the RBS data. In the triple-layer model after annealing of the Ni/a-C stack, the areal densities of Ni and C are $d_{Ni,\,out} = 72\times10^{15} + 517\times10^{15} = 589\times10^{15}$ at. cm^{-2} and $d_{C,out} = 590\times10^{15} + 102\times10^{15} = 692\times10^{15}$ at. cm^{-2}, respectively. In the triple-layer model after annealing of the a-C/Ni stack, the areal densities of Ni and C are $d_{Ni,\,in} = 431\times10^{15} + 45\times10^{15} = 476\times10^{15}$ at. cm^{-2}

and $d_{C,\,in}$ = 43×10^{15} + 640×10^{15} = 683×10^{15} at. cm^{-2}, respectively. The total areal densities for both samples after annealing are in full agreement with those of the as-deposited samples within the experimental accuracy.

Additional information about the distribution of the elements was obtained from the elastic recoil detection analysis. In contrast to RBS, ERDA allows a more precise determination of the carbon concentration because of its higher sensitivity and lower detection limit for light elements. This is illustrated in particular by the rectangular shape of the concentration profiles of nickel and by the steep gradient of the carbon concentration in as-deposited samples (Figs. 2a and 2c).

The concentration profiles of Ni and C in the annealed Ni/a-C layer stack have almost the same form (Fig. 2b) like in the as-deposited sample, which confirms a complete LE that was already suggested by the RBS analysis. In the annealed a-C/Ni stack, the positions of the Ni and C depth profile maxima are also inverted, as expected for LE. However, in contrast to the LE in the outward direction, the profiles are broadened, which might be an indicator of the intermixing of elements.

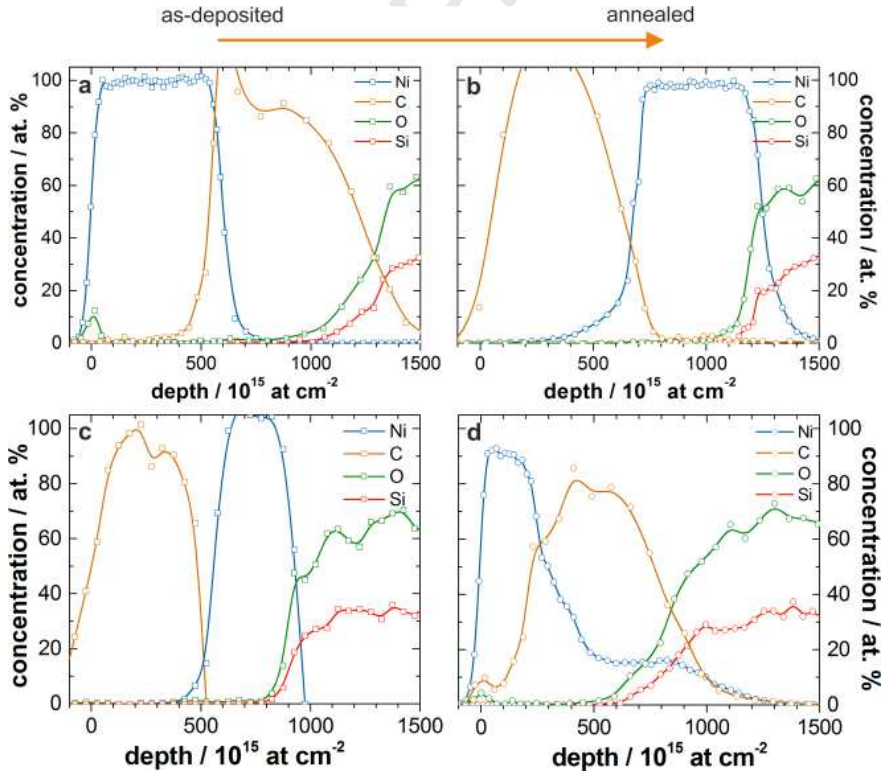

Figure 2: ERD depth profiles of the as-deposited and annealed Ni/a-C (a, b) and a-C/Ni (c, d) layer stacks. The points represent the measured data; solid lines are a guide for the eye. Near the Ni layer, the depth profiles for the lighter elements seem to increase rapidly and to have a concentration higher than 100 %. This artefact is caused by a drastic change in the stopping force between the metal and the C layers and by the limited detector resolution. The profiles seem to extend above the surface and Ni profiles have long tails towards the substrate. These effects are caused by limited detector resolution, multiple scattering, straggling effects and thickness variation.

The layer exchange in both stacks was confirmed by TEM (Fig. 3). Furthermore, the TEM micrographs revealed that the incomplete LE in the a-C/Ni stack is accompanied by an increase of the interface roughness (Fig. 3d). One can clearly see that the Ni/c-C interface is much rougher for the inward LE (Fig. 3d) than for LE in the outward direction (Fig. 3b). Moreover, few Ni crystallites still stuck at the substrate (Fig. 3d). This interface roughness was recognized by ERDA as a wide transition zone in the depth between 200×10^{15} and 400×10^{15} at. cm^{-2} (Fig. 2d). After implementing this roughness into the model for the simulation of the RBS spectra significantly better agreement between experimental data and model was achieved.

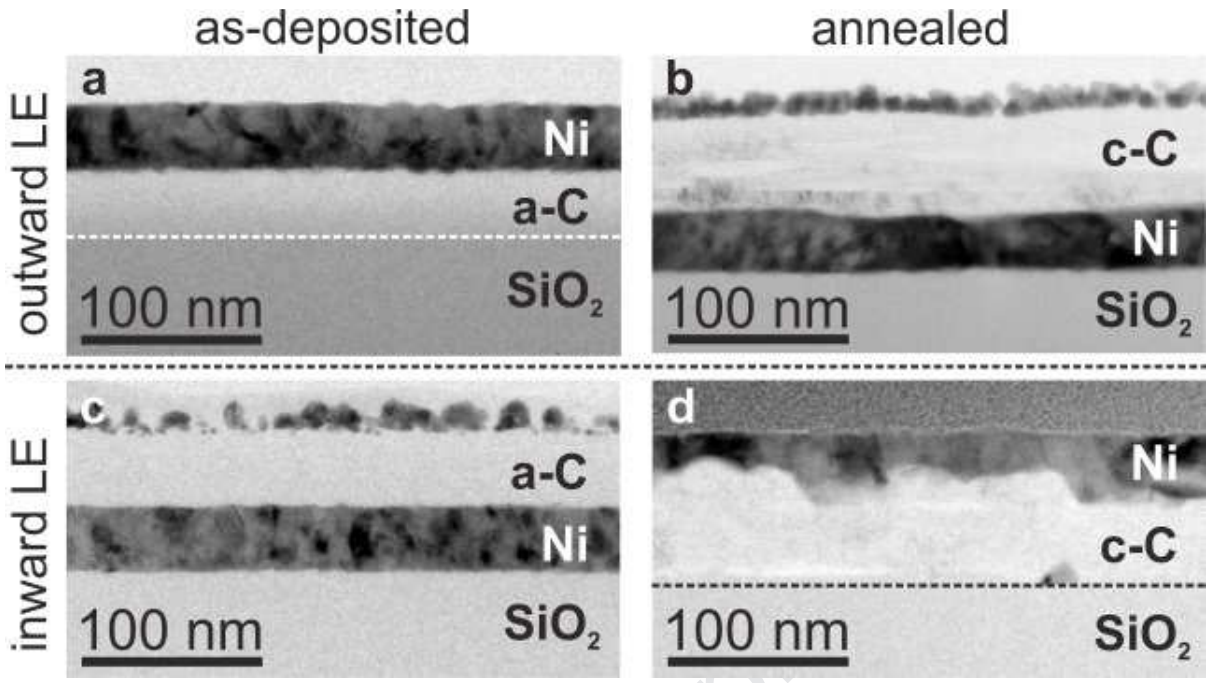

Figure 3: TEM micrographs of the Ni/a-C and a-C/Ni bilayer stacks before (a, c) and after (b, d) the annealing. Because of their low image contrast, the C/SiO_2 interfaces are highlighted by dashed lines.

3.2. Degree of the layer exchange

In order to quantify the LE, a degree of layer exchange α_{LE} was calculated for both stacking sequences from RBS and elastic recoil detection (ERD) data. The LE degree has recently been introduced as the relative amount of C or Ni atoms that diffused through the adjacent Ni or C layer[23]. It is a measure of the LE completeness and calculated from the ratio between the amounts of exchanged and remaining species in the respective layer. The values of α_{LE} are summarized in Table 1.

For the calculation of α_{LE} from the RBS data, the spectra (Fig. 1) were fitted with a multi-layer sample model.[28] Before annealing, the individual layers were simulated by single elements (Ni and C), and a small amount of Ar (see section 3.1). After annealing, the elemental profiles were composed of the exchanged elements with a residual amount of the original species, in order to be able to reproduce the asymmetric profiles in Fig. 1b. The percentage of the

exchanged elements has been used to calculate α_{LE}. The good agreement of the integrated intensity of the RBS peaks measured before and after annealing has confirmed the mass conservation.

Table 1: Layer exchange degree α_{LE} based on C and Ni in a-C and Ni bilayer stacks as determined by RBS and ERDA.

	method	α_{LE}^{C}	α_{LE}^{Ni}
outward LE	RBS	91 ± 5 %	98 ± 2 %
	ERDA	95 ± 2 %	98 ± 2 %
inward LE	RBS	80 ± 10 %	76 ± 7 %
	ERDA	86 ± 5 %	88 ± 5 %

Concurrently, the α_{LE} was determined from the concentration depth profiles, which were obtained from the fitting of the ERD spectra using the code developed by Barradas et al.[29] For the calculation of α_{LE} from ERDA, concentration values displayed in Fig. 2 were integrated over the depth. The layer thicknesses obtained from the RBS multi-layer model and given in at. cm^{-2} (Section 3.1) were used as integration limits.

The differences in α_{LE} (Table 1) clearly illustrate the dependence of the LE degree on the sequence of the Ni and C layers in the Ni/a-C and a-C/Ni stacks. The LE directionality was additionally proven by an annealing experiment that was carried out on a triple-layer stack (Ni/a-C/Ni) under the same conditions as for the bilayers. Before annealing, the depth profiles of the Ni concentration measured using ERDA were almost rectangular with a small interface roughness (Fig. 4a), as expected for sequentially deposited Ni and a-C layers. After annealing, a major part of carbon had moved towards the sample surface, while only a minor part of carbon diffused towards the substrate (Fig. 4b). Like in the a-C/Ni layer stack (Figs. 1b, 2d and 3d), a certain fraction of Ni does not participate in the layer exchange and adheres to the substrate during annealing (see supplementary information for RBS depth profiles of the triple

layer stack).

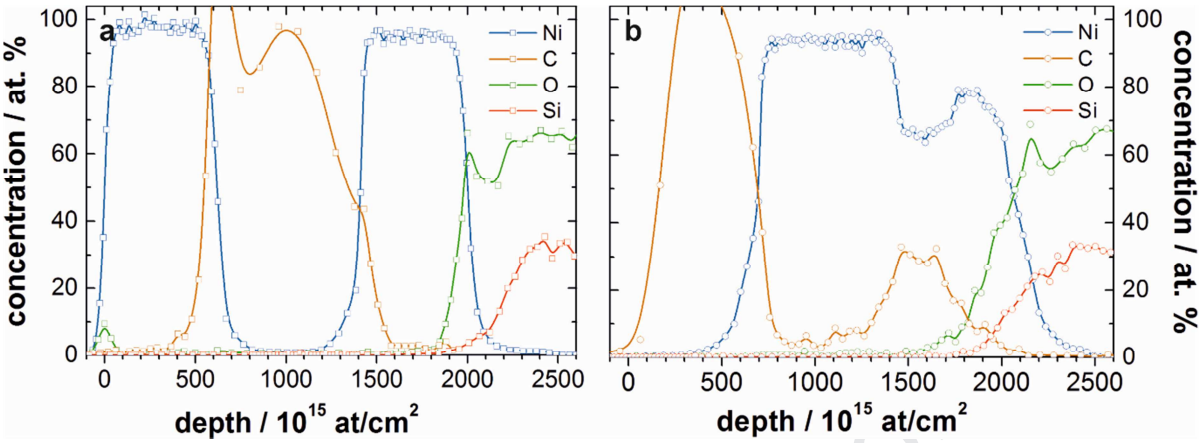

Figure 4: ERD depth profiles of the as-deposited (a) and annealed (b) Ni/a-C/Ni triple layer. The points represent the measured data; solid lines are a guide for the eye.

3.3. Nickel-induced crystallization of carbon

Raman spectra of the as-deposited carbon layers (Figs. 5a and 5d) exhibit a broad band comprising a shoulder at 1350 cm^{-1} and a peak at ≈ 1535 cm^{-1}. These features represent the D and G line of small sp^2-C ring clusters in both initial a-C films.[32,33] The I_D/I_G ratios of both initial stacks, a-C/Ni and Ni/a-C, are estimated to be ≈ 0.5. This indicates identical amorphous carbon structures as precursors of the layer exchange (Figs. 5a and 5d).[32,33]

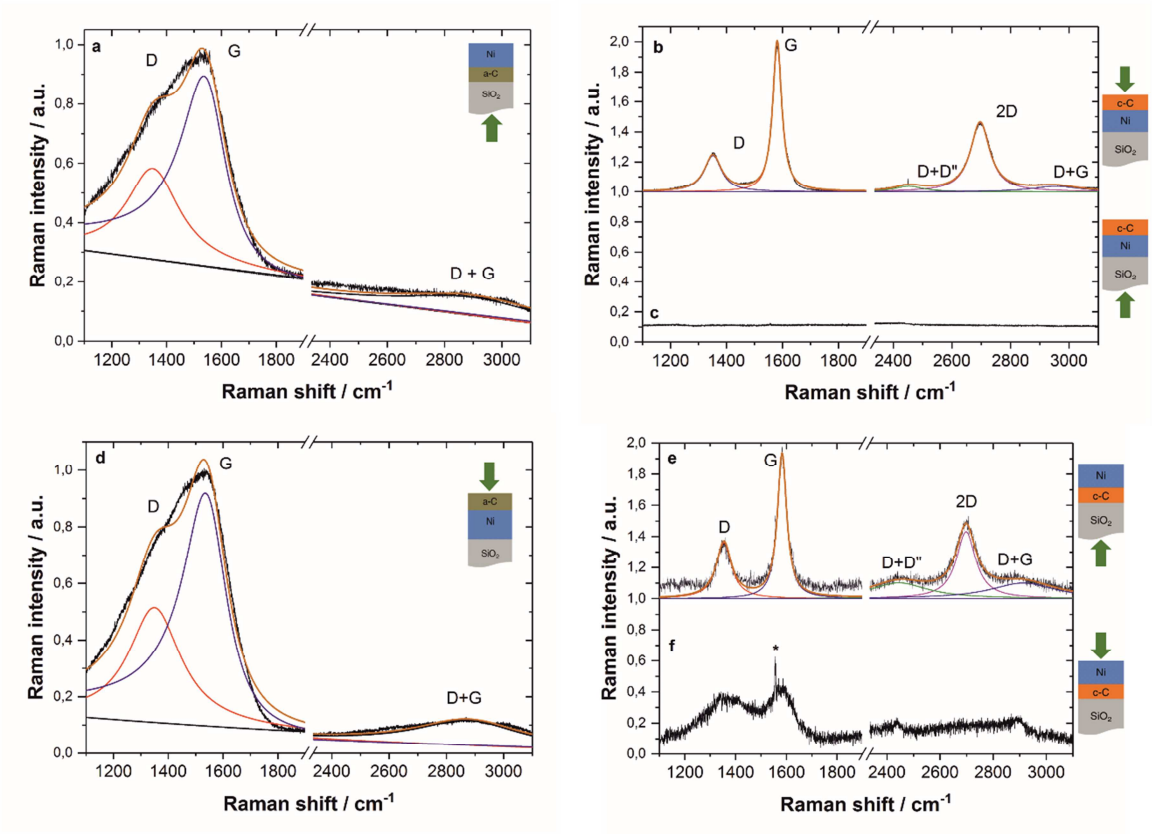

Figure 5: Raman spectra of the Ni/a-C and a-C/Ni bilayer stacks before and after annealing measured from the top and through the transparent SiO_2 substrate (i.e., from the backside of the stack). a) As-deposited Ni/a-C measured through the substrate, b) annealed Ni/a-C measured from the top, c) annealed Ni/a-C measured through the substrate. d) as-deposited a-C/Ni measured from the top, e) annealed a-C/Ni measured through the substrate, f) annealed a-C/Ni measured from the top. The green arrows in the stack drawings indicate the propagation direction of the exciting laser radiation. The asterisk in image f) marks the ambient oxygen signal.

In the annealed samples, Raman spectroscopy was mainly used as a proof of the carbon crystallization. The positions and widths of the Raman lines are summarized in Table 2. The D and G lines became narrower and shifted towards wave numbers typical for graphenic carbon. The most important structure indicator is the presence of the characteristic 2D line in the spectra of both layer stacks after annealing (Figs. 5b and 5e). In both stacks, the 2D line showed no

side peaks or shoulders and was fitted using a single Lorentzian function. The single, non-split 2D line points to graphenic structures without ordering of the basal planes in the *c* direction, i.e., monolayer graphene or turbostratic carbon[34-41] (cf. Table 2). The glassy carbon reference material, SIGRADUR® G, is a commercial form of turbostratic carbon heated to above 2200°C during preparation. From the three reference structures (Table 2), monolayer graphene is excluded by the carbon layer thickness. The Raman spectra of the annealed samples suggest that the crystallized carbon resembles turbostratic carbon in both bilayer stacks. I.e., the initial Ni/a-C stack has transformed into c-C/Ni, and the initial a-C/Ni into Ni/c-C, where c-C represents turbostratic carbon.

Table 2: Raman fit parameters for the Ni/a-C and a-C/Ni bilayer samples after LE in comparison to those of representative reference materials. The glassy carbon was delivered by HTW Germany (n.a.: not available).

	D line (cm^{-1})		G line (cm^{-1})		2D line (cm^{-1})		I_D/I_G	I_{2D}/I_D
	position	FWHM	position	FWHM	position	FWHM		
outward LE	1350	63.6	1578	42.7	2692	80.0	0.27	2.4
inward LE	1352	73.5	1581	46.4	2698	85.7	0.34	1.3
turbostratic carbon[40]	1344	30.3	1582	19.2	2707	42	0.21	n.a.
glassy carbon	1346	52.6	1585	40.6	2692	72.5	2.21	1.5
graphene on quartz[42]	-	-	1582	16	2675	29	-	-

Still, the presence of the 2D line in the Raman spectra of annealed samples indicates the formation of in-plane long-range ordered graphenic planes[35,43] (Fig. 5). The mean lateral crystallite size of the graphenic domains ($\boldsymbol{L_a}$) was estimated from the I_D/I_G ratio by applying the Tuinstra-König relation[41,44,45] to be approximately 16 nm and 13 nm for the outward and in-

ward LE direction, respectively. Since this relationship is based on the correlation with X-ray data, these values reflect the crystallite size of defect-free graphenic areas. For the outwards LE direction, the area of these domains is approx. 1.6-times larger than for the inwards LE direction. A higher structural in-plane ordering of the graphenic domains after the LE in the outwards direction is furthermore reflected by the higher I_{2D}/I_D ratio and the narrower line widths (Table 2).

X-ray diffraction revealed that the interplanar spacing of the graphenic planes of the obtained turbostratic carbon, d_{002} = (0.3403 ± 0.0002) nm, is 1.4 % larger than the distance of the basal planes in 2H graphite, i.e., d_{002} = 0.3356 nm[46]. From the broadening of the diffraction line 002, the coherent size of the turbostratic carbon in the *c* direction ($\boldsymbol{L}_c$) was estimated using the Scherrer equation[47] to be about 10 nm for both layer exchange directions. The observed values agree with those reviewed for turbostratic carbon, d_{002} = 0.338 - 0.342 nm and $\boldsymbol{L}_c$ = 6 - 20 nm.[3] A further consequence of the carbon crystallization was the increase of the total sample thickness that was observed by HRTEM for both LE directions (Fig. 3).

In agreement with the results of Raman spectroscopy, TEM detected planar graphenic planes parallel to the Ni surface throughout the layer after outward LE and the superposition of parallel planar and curved planes after inward LE (Fig. 6 b, d). The latter finding can be attributed to the restructuring of the Ni layer during the LE and might be an indication of three-dimensional growth of c-C at the interface close to the substrate.

For verification of the LE completeness and/or for the detection of non-exchanged carbon, Raman measurements were also carried out on the Ni side of the annealed samples. In the annealed Ni/a-C stack, no carbon signal was detected at the interface between the substrate and the Ni layer (Fig. 5c), which confirms the complete LE in the outward direction that was concluded from the RBS and ERDA (Table 1). In contrast to that, a small fraction of disordered carbon persisted at the sample surface during the layer exchange in the inward direction (a-C/Ni stack, Fig. 5f). In this context, it is worth noting that Raman spectroscopy is capable of detecting a-C carbon layers having a thickness of 1 nm or less[48]. The incomplete LE in the inward direction was already indicated by a low α_{LE} (Table 1). The weak Raman spectrum at the sample surface of a-C/Ni after annealing (Fig. 5f) shows six-fold sp^2-C ring cluster without

long-range ordered graphenic planes.[13] This type of spectrum is typical for thermally annealed, non-crystallized amorphous carbon.

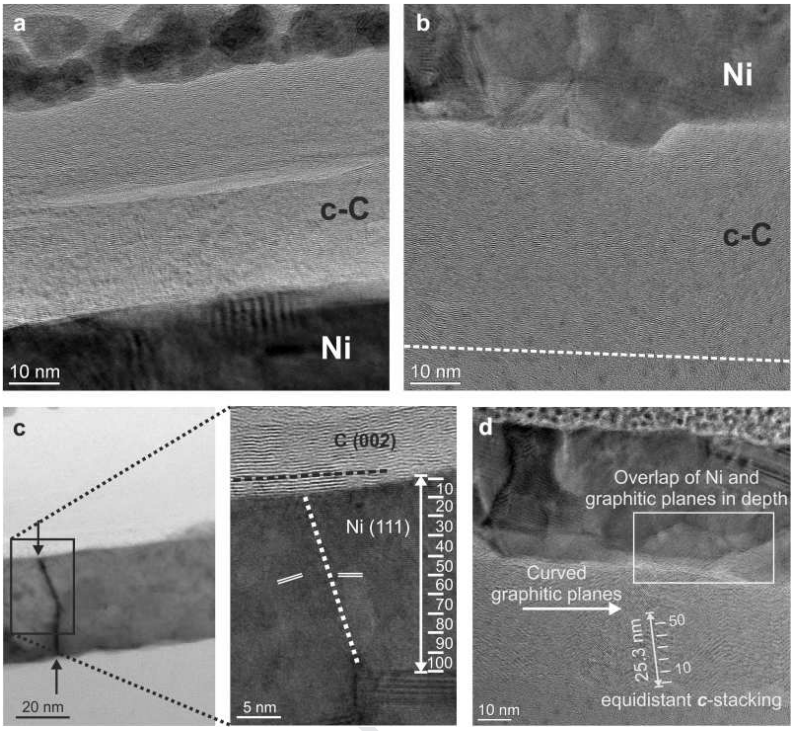

Figure 6: TEM micrographs of the Ni/a-C (a) and a-C/Ni (b) layer stacks after annealing. They demonstrate the microstructure of the crystallized carbon (c-C) and the morphology of the c-C/Ni and Ni/c-C interfaces. The dashed line in figure (b) mark the c-C/SiO_2 interface, which is hardly visible due to a low image contrast. Figure (c) shows parallel graphenic planes formed across the Ni GB after outward LE. Here, Ar-filled pillow-shaped features occurred after lamella preparation. Figure (d) shows the coexistence of planar and curved graphenic planes after inward LE.

3.4. Microstructure changes in the nickel layers

X-ray diffraction confirmed the crystallinity of the Ni layers both in the as-deposited and annealed state. The size of Ni crystallites in the bilayer stacks under study was determined from XRD line broadening using the modified Williamson-Hall analysis[49] to be

(10.5 ± 2.0) nm and (23.5 ± 1.6) nm before and after annealing, respectively. The increase of the crystallite size was independent of the LE direction. The Williamson-Hall analysis has shown the absence of microstrain for all samples.

The analysis of the lattice parameters calculated from the positions of individual diffraction lines of Ni revealed that the as-deposited stacks are almost free of residual stress, while the annealed stacks show a tensile residual stress (Fig. 7, Tab. 3). Furthermore, the dependence of the measured lattice parameters of Ni on the diffraction indices, caused by the crystal anisotropy of the elastic constants, was overlaid by another *hkl*-dependence that originated from the presence of the stacking faults (SFs) on the {111} lattice planes of Ni.[50] In order to account simultaneously for presence of SFs and for crystallographic anisotropy of the elastic constants, the measured lattice parameters (a_{ψ}^{hkl}) were fitted by the function [51,50,52,53]

$$a_{calc}^{hkl}(\psi) = a_0 \left[\sigma f_{hkl}(\psi) - \alpha_{SF} \frac{\sqrt{3}}{4\pi} G_{hkl} + 1 \right]. \qquad (1)$$

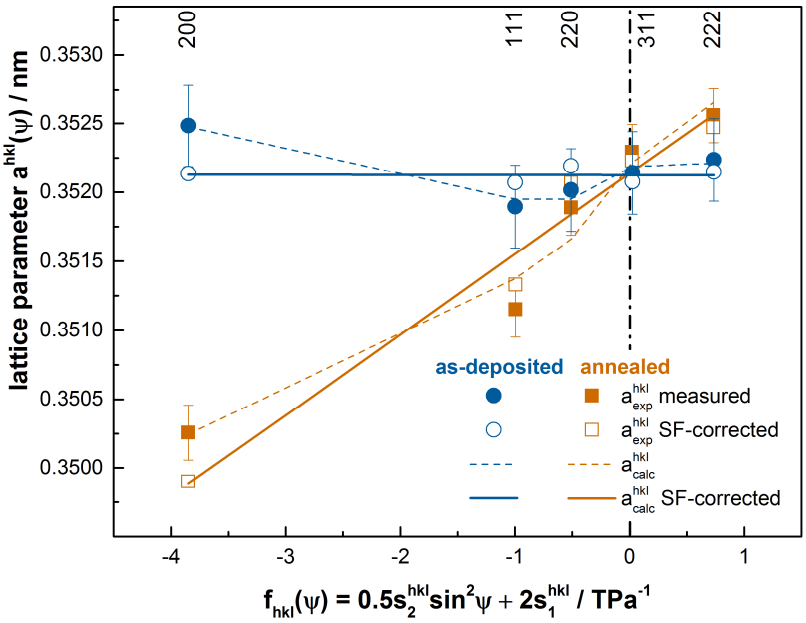

Figure 7: Dependence of the measured and SF-corrected lattice parameters on the function *f(ψ)* for the Ni/a-C stack before and after annealing.

Refinable parameters in Eq. (1) are the stress-free lattice parameter (a_0), the residual stress (σ) and the stacking fault probability (α_{SF}). The function

$$f_{hkl}(\psi) = \tfrac{1}{2}s_2^{hkl}\sin^2\psi + 2s_1^{hkl} \qquad (2)$$

describes the effect of the residual stress on the measured lattice parameters in elastically anisotropic materials. ψ is the angle between the sample surface normal and the diffraction vector. The X-ray elastic constants $\frac{1}{2}s_2^{hkl}$ and $2s_1^{hkl}$ were calculated from the single-crystal elastic constants of nickel, S_{11} = 7.5 × 10^{-12} Pa^{-1}, S_{12} = -2.86 × 10^{-12} Pa^{-1} and S_{44} = 8.16 × 10^{-12} Pa^{-1}, using the Reuss approach.[54,55] The values of $\frac{1}{2}s_2^{hkl}$ are 4.08 TPa^{-1}, 10.4 TPa^{-1}, 5.65 TPa^{-1}, 7.40 TPa^{-1} and 4.08 TPa^{-1} for the diffraction lines 111, 200, 220, 311 and 222, respectively. The values of $2s_1^{hkl}$ are -1.53 TPa^{-1}, -5.72 TPa^{-1}, -2.58 TPa^{-1}, -3.74 TPa^{-1} and -1.53 TPa^{-1} for the same sequence of diffraction lines. The function

$$G_{hkl} = \frac{\sum_{hkl}[k_{hkl}(h+k+l)]}{m_{hkl}(h^2+k^2+l^2)} \qquad (3)$$

describes the 'contrast factor' of the {111} stacking faults in fcc materials[50]. The factor k_{hkl} in Eq. (3) is equal to +1 for $(h+k+l)$ mod 3 = 1 and to −1 for $(h+k+l)$ mod 3 = 2. For $(h+k+l)$ mod 3 = 0, $k_{hkl} = 0$.[53,49] m_{hkl} is the multiplicity of the lattice planes {hkl}. For the diffraction lines 111, 200, 220, 311 and 222, the contrast factors of stacking faults (G_{hkl}) are equal to 1/4, -1/2, 1/4, 1/11 and -1/8, respectively.

Table 3: Residual stress σ and the stress-free lattice parameter a_0 in Ni before and after annealing for both stacking sequences.

	σ (GPa)		a_0 (nm)
	outward LE	inward LE	
as-deposited	-0.0 ± 0.1	0.2 ± 0.1	0.3521 ± 1×10^{-4}
annealed	1.7 ± 0.2	1.4 ± 0.2	0.3521 ± 2×10^{-4}

The stress-free lattice parameter of Ni remained unchanged after annealing (Tab. 3). It was not altered by the LE, although a small amount of C atoms (approx. 0.5 % C) may be dissolved in Ni at 700 °C[17]. The incorporation of 0.5 % of C on interstitial positions would increase the lattice parameter by about 0.085 % [56], which was not observed experimentally. Thus, the LE mechanism via C diffusion through the Ni layer can be excluded. However, the stress-free lattice parameter of Ni is slightly below the reference value of 0.3524 nm (ICDD PDF(2019) 00-004-0850), but it is in good agreement with the lattice parameters reported by Sheng et al.[57] and Radic et al.[58] for nanocrystalline Ni.

The formation of SFs in as-deposited samples is apparently facilitated by the small thickness of the Ni layers. The occurrence of SFs in fcc structures is frequently regarded as a first step towards a transition to a hexagonal close packed phase[50,59]. This approach is also applicable for nickel. Its metastable hexagonal phase was observed in thin films by Hemenger & Weik[60] and by Wright & Goddard[61]. The effect of the stacking faults on the measured lattice parameters is illustrated exemplarily in Fig. 7 for the Ni/a-C stack, where the presence of SFs leads to a violation of the linear dependence of the lattice parameters on $f_{hkl}(\psi)$. The SF-corrected lattice parameters $a_{exp}^{hkl}(\psi)(corr.)$ were calculated using $a_{exp}^{hkl}(\psi)(corr.) = a_{exp}^{hkl}(\psi) + a_0\alpha_{SF}G_{hkl}\sqrt{3}/4\pi$ with the parameters a_0 and α_{SF} that were obtained from Eq. (1). The presence of SFs before and after the LE was observed also in stacks with the inverse order of carbon and nickel layers. The SF probability determined using Eq. (1) was about 1 % for all investigated samples. The relatively low annealing temperatures appears to be insufficient for SF annihilation, thus the relaxation of SFs upon annealing is suppressed.

The flat a_{ψ}^{hkl} vs. $f_{hkl}(\psi)$ dependence observed for the as-deposited Ni layer is typical for an almost stress free material. In contrast, the positive slope obtained for annealed layer stacks, i.e. after LE, (Fig. 7) indicates rather high tensile stress. A possible source of this stress are different thermal expansion coefficients of fcc-Ni (18.3×10^{-6} K^{-1})[62] and nanocrystalline graphite (0.9×10^{-6} K^{-1}).[63] Assuming a perfect cohesion of both layers and solely elastic deformation of both counterparts, the difference in the thermal expansion coefficients would lead to a total in-plane lattice deformation of approx. 1.2 % upon cooling from 700 °C to RT. The effective in-plane elastic lattice deformation in annealed Ni layers, which was calculated as the relative

difference between the extrapolated in-plane lattice parameter $a_{\parallel}$ and the stress-free lattice parameter a_0,

$$\varepsilon = \frac{a_{\parallel} - a_0}{a_0}, \qquad (4)$$

was found to be in the range between 0.5 % and 0.7 % for all annealed layer stacks.

3.5. Model of the layer exchange

RBS, ERDA and Raman spectroscopy revealed that annealing to 700 °C results in the LE of carbon and nickel in a-C/Ni, Ni/a-C and Ni/a-C/Ni stacks, and that the layer exchange is accompanied by the metal-induced crystallization of amorphous carbon. Possible paths for the layer exchange are (i) volume diffusion of carbon through the nickel crystallites and (ii) carbon diffusion along GBs between the Ni crystallites.

A negligible volume diffusion of carbon through Ni crystallites was implied by the conservation of the Ni lattice parameter (Section 3.4). Noteworthy, LE via diffusion of C through Ni crystallites is less probable, because of a low solubility of carbon in nickel[17] and a slow diffusion in three dimensions as compared with a two-dimensional diffusion along GBs.[64,65] Moreover, the activation energy of the bulk diffusion (1.62 eV) is substantially larger than the activation energy of the GB diffusion (0.77 eV).[65] In case of a dissolution-precipitation mechanism, the graphenic structures are expected to form on both sides of the catalyst layer. This is not in agreement with our observations. Therefore, GB diffusion is regarded as the dominant diffusion mechanism during the layer exchange.

The GB diffusion of carbon is corroborated by a small lateral size of graphenic domains (16 nm and 13 nm for the outward and inward LE direction, respectively) that was obtained from the ratio of the D and G peaks in the Raman spectra (Section 3.3). The presence of GBs in the nanocrystalline Ni layer as well as the comparable lateral size size (~10nm) of Ni crystallites and of the graphenic domains are visually confirmed in the TEM micrographs (Fig. 3, Fig. 6). The HRTEM micrographs (Fig. 6) evidenced formation of tiny fissures, which can serve as paths for enhanced carbon diffusion. The formation of such fissures is facilitated by the formation of tensile stresses in annealed samples (Section 3.4).

Based on the results of RBS, ERDA, Raman spectroscopy, XRD, TEM, and HRTEM, the following model of the Ni-induced crystallization of a-C with layer exchange can be formulated and is sketched in Figure 8. The LE takes place mainly via C diffusion along the Ni grain boundaries and is driven by the crystallization of a-C. According to the existing mechanistic concepts of MIC[11], the covalent bonds between the C atoms are screened by the electron gas of the adjacent Ni grains up to a depth of two atomic layers. As a consequence of this Coulomb screening, a thin layer of mobilized C atoms is formed.[11] At sufficiently high temperatures, the mobilized C atoms diffuse along the Ni GBs to the opposite Ni interface (between Ni and vacuum or substrate). The contribution of C diffusion through Ni crystallites to the layer exchange is negligible. The GB wetting is independent of the initial stacking sequence, because the interfaces involved in this elementary step are the same for both LE directions.

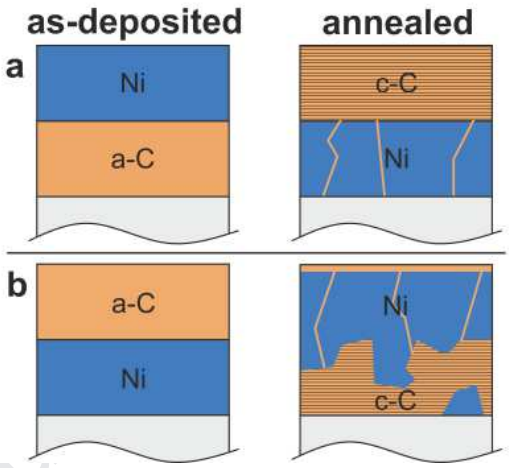

Figure 8: Schematic picture of the initial and final states of the Ni/a-C (a) and a-C/Ni (b) stacks before (left) and after the LE (right), according to the proposed LE mechanism. Orange lines within the Ni layer indicate Ni GBs.

RBS, ERDA, Raman spectroscopy and HRTEM experiments revealed that the degree of the LE (α_{LE}) depends on the sequence of Ni and C layers in the original stack and that the roughness of the Ni/c-C interfaces increases after LE. The increase of the interface roughness depends on the sequence of the Ni and C layers in the original stack as well. A phenomenon appearing in the inward direction was a lateral heterogeneity of the Ni layer (Figs. 3d and 6d).

The structure of crystallized carbon was found to be different for different LE directions. For the outward LE, graphenic layers with a larger in-plane domain size and a strongly preferred orientation parallel to the Ni surface are formed. These conclusions were suggested by the results of Raman spectroscopy (Section 3.3) and confirmed by HRTEM (Figs. 6a and 6c). For the inward LE, carbon atoms have to diffuse into the Ni/SiO_2 interface. The splitting of this interface requires additional energy, thus the two-dimensional growth is restricted in comparison with the crystallization occurring at the sample surface. A continuous supply of mobilized C atoms through the GBs and the expansion of the turbostratic carbon layer in the constrained space between Ni and the substrate leads to the formation of folded or curved graphenic planes (Fig. 6b, d) and to the increase of the roughness of the Ni/C interfaces (Fig. 3d).

4. Discussion

The mechanisms of the layer exchange and metal-induced crystallization of Ni/a-C and a-C/Ni bilayers proposed in Section 3.5 can be substantiated by thermodynamic considerations and by comparing the surface and interface energies of the counterparts. The standard formation enthalpy is always lower for crystallized carbon than for a-C. The difference in the standard formation enthalpies gives the reaction enthalpy of crystallization, which ranges between 20 and 100 kJ/mol, depending mainly on the initial state of the disordered carbon.[3,18,66] Consequently, the crystallization of a-C is a thermodynamically driven process, which becomes catalysed, if a-C gets in contact with Ni[3,6,11]. The phenomena needing more explanation are the LE, which accompanied the crystallization of a-C in all samples under study, and the dependence of the LE on the sequence of Ni and a-C in the bilayer stacks.

Assuming that LE occurs via Ni-GB diffusion, the mobilized C atoms form two Ni/a-C interfaces, which replace original GBs in Ni. Not every GB is available to serve as a diffusion path as the energy of a `double´ Ni/a-C interface ($2 \times \gamma_{Ni/a-C}^{int}$ = 1.368 J/m²) is lower than the GB energy of Ni ($\gamma_{Ni}^{GB} \cong$ 1.3 to 1.6 J/m²; in dependence of the GB inclination and geometrical factor used in the derivation of the grain boundary energies).[67,68] The experimental results, however, indicate that the majority of the Ni GBs are involved in the LE process as diffusion

paths, since the size of c-C crystallites is small (13 – 16 nm) and in a reasonable agreement with the lateral crystallite size of nanocrystalline sputtered Ni thin films at room temperature.[58,69] The wetting of Ni GBs by carbon (accompanied by diffusion along the GBs) lowers the total energy of the system[70] and is independent of the LE direction. The surface and interface energies were calculated following the approach presented by Wang[70] and Sommer[71] for the annealing temperature of 700 °C and are listed together with further interface and surface energies in Table 4. Figure 9 displays the dependence of these energies on the temperature.

Table 4: Surface and interface energies at 700 °C in the Ni and C layer stacks calculated using the approach presented by Wang[76] and Sommer[77]. The calculated values are given in J/m².

Ni	a-C	c-C	SiO_2
$\gamma_{Ni}^{s} = 2.314$[72]	$\gamma_{Ni/a-C}^{int} = 0.684$[72-74]	$\gamma_{Ni/c-C}^{int} = 0.999$[72,74,75]	$\gamma_{Ni/SiO_2}^{int} = 0.158$[72,76,77]
	$\gamma_{a-C}^{s} = -0.064$[73]	no interface	$\gamma_{a-C/SiO_2}^{int} = 1.145$[73,76,78]
		$\gamma_{c-C}^{s} = 0.026$[75]	$\gamma_{c-C/SiO_2}^{int} = 1.873$[75,76,78]

During LE in outward direction, the LE is mediated by the energetically favourable wetting of the Ni GBs by carbon atoms and the Ni surface has to be replaced by two new interfaces: Ni/c-C and c-C/vacuum. For a temperature of 700°C, the sum of the resulting energies, $\gamma_{Ni/c-C}^{int}$ and γ_{c-C}^{s}, is significantly lower than the surface energy of nickel in the initial state (γ_{Ni}^{s}). Therefore, the decrease of the total interfacial energy ($\Delta\gamma$ = -1.289 J/m²) is an essential component of the driving force for the layer exchange. Furthermore, in agreement to the complete LE outwards, the a-C/SiO_2 interface is replaced by the Ni/SiO_2 interface, which further reduces the total energy ($\Delta\gamma$ = -0.987 J/m²). As carbon can crystallize at the originally free Ni surface, the outward LE leads to the formation of a flat c-C/Ni interface.

For inward LE, the total energy of the system is only reduced by the wetting of the Ni GBs by carbon and by the crystallization of a-C. The replacement of the Ni/SiO_2 interface by the Ni/c-C and c-C/SiO_2 interfaces ($\gamma_{Ni/c-C}^{int} + \gamma_{c-C/SiO_2}^{int} - \gamma_{Ni/SiO_2}^{int}$ = 2.714 J/m²) and the formation of a Ni surface (γ_{Ni}^{s}) are connected with an increase of the total interfacial energy (see

Tab. 5). The primary consequence of this energy balance is the experimentally observed lower LE degree in the inward direction than in the outward direction. In addition to the higher energy demand for the splitting of the initial Ni/SiO_2 interface, the higher interface energies after inward LE contribute to the formation of corrugated c-C planes as seen by Raman spectroscopy and TEM. The expansion of the c-C layer due to the ordering further promotes the restructuring of the Ni/c-C interface. Since the exposure of the Ni layer to vacuum would lead to an increase of the surface energy, the formation of the Ni surface is avoided and a thin a-C layer persists at the surface of the sample after inward LE (Fig. 5).

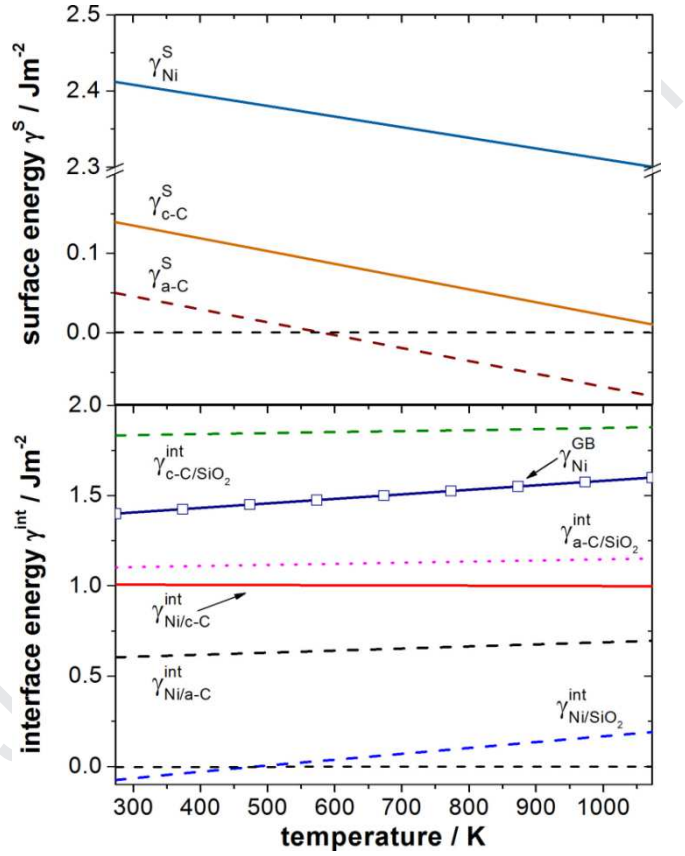

Figure 9: Calculated surface γ^S and interface energies γ^{int} of the presented layer stacks and Ni GB energy as a function of temperature.

While for outward LE a turbostratic carbon structure is formed by two-dimensional growth, a complex microstructure characterized by the coexistence of planar and curved graphenic

basal planes (Fig. 6d) and by the mutual penetration of c-C and Ni layer (Fig. 3d) is formed during inward LE. For nucleation and lateral growth, a higher amount of interface energy is necessary, compared to the outward LE (Fig. 9 and Tab. 4). Under the given conditions, two-dimensional growth of turbostratic carbon at the former Ni/SiO_2 surface is restricted, while the supply of C atoms is not affected. The crystallization starts inside the Ni GBs, as soon as the critical thickness for crystallization is reached, gradually restructuring the Ni/c-C interface[70]. Therefore, the two-dimensional growth of graphenic planes along the SiO_2 substrate occurs concurrently with the three-dimensional growth inside the Ni GBs, similar to the MIC between a-Si and Ag[27]. In addition, the lateral and vertical expansion of the c-C layer encapsulated between Ni and the substrate lead to the folding of graphenic planes (Fig. 3 and 6).

The temperature dependence of the surface and interface energies (Fig. 9) demonstrates the validity of the proposed mechanism in the investigated temperature range (500 – 700 °C). The dependences of the surface energies on temperature possess almost the same slopes for Ni, c-C and a-C, thus the contribution of these species to the energy balance is mutually temperature-independent. The energies of the Ni/SiO_2 and Ni/a-C interfaces increase slightly with increasing temperature, while the Ni/c-C interface energy slightly decreases. However, these changes do not change the relationships explained in detail for 700 °C. The negative interface energy between Ni and the substrate below roughly 450 °C is in good agreement with the enhanced wetting of the substrate by the Ni layer at low deposition temperatures and the formation of Ni drops during the sputtering at elevated temperatures[79].

5. Conclusions

This study has quantified general and directional features of the Ni-catalysed layer exchange and metal-induced crystallization in a-C/Ni, Ni/a-C and Ni/a-C/Ni thin film stacks grown on fused silica and thermally oxidized Si. The common driving forces in both LE directions were the crystallization of a-C and the wetting of Ni grain boundaries by carbon. During outward LE, an almost complete LE ($\alpha_{LE} \approx 93$ %) occurred, additionally driven by the decrease of the total interfacial energy during the process. This layer exchange results in the formation of turbostratic carbon throughout the entire C layer, whose basal planes are aligned parallel to the

sample surface. For inward LE, the less favourable interfacial energy contributions result in a lower α_{LE} (≈ 83 %), in the restructuring of the Ni layer and in the competition of two- and three-dimensional growth. Moreover, the graphenic basal planes have a slightly smaller lateral extension after inward LE.

The experimental findings were substantiated by thermodynamic considerations based on comparison of the surface and interfacial energies of the initial and final states. They have shown that the initial and final reaction states are decisive for the direction-dependent structural quality of exchanged carbon and LE degree in the a-C/Ni thin film stacks. Moreover, the thermodynamic estimations have confirmed the crystallization in combination with the decrease of the interface energies as the main driving forces for the LE.

The consistency of experimental results and thermodynamic estimations is very encouraging, as it offers a possibility to design layer stacks with desired microstructure of turbostratic carbon after the layer exchange.

Acknowledgments

Support by the Ion Beam Center at HZDR is gratefully acknowledged. The authors thank A. Erbe, R. Heller and P. Zahn from Helmholtz-Zentrum Dresden-Rossendorf for helpful discussions. J. Zscharschuch, A. Schneider, R Aniol and A. Scholz are gratefully acknowledged for technical assistance. This work was financially supported by the Initiative and Networking Funds of the president of the Helmholtz Association via the W2/W3 program (SG).

References

1 Robertson, J. Amorphous-Carbon. *Advances in Physics* **35**, 317-374, doi:10.1080/00018738600101911 (1986).

2 Franklin, R. E. Crystallite Growth in Graphitizing and Non-Graphitizing Carbons. *Proc R Soc Lon Ser-A* **209**, 196-&, doi:10.1098/rspa.1951.0197 (1951).

3 Ōya, A. & Marsh, H. Phenomena of catalytic graphitization. *Journal of Materials Science* **17**, 309-322, doi:10.1007/bf00591464 (1982).

4 Lamber, R., Jaeger, N. & Schulz-Ekloff, G. Electron microscopy study of the interaction of Ni, Pd and Pt with carbon. *Surface Science* **197**, 402-414, doi:10.1016/0039-6028(88)90636-x (1988).

5 Berndt, M. *et al.* Bulk diffusion induced structural modifications of carbon-transition metal nanocomposite films. *Journal of Applied Physics* **109**, 063503, doi:10.1063/1.3559302 (2011).

6 Marsh, H. & Warburton, A. P. Catalysis of graphitisation. *Journal of Applied Chemistry* **20**, 133-142, doi:10.1002/jctb.5010200409 (1970).

7 Ching Li, P. Preparation of Single-Crystal Graphite from Melts. *Nature* **192**, 864-865, doi:10.1038/192864a0 (1961).

8 Austerman, S. B., Myron, S. M. & Wagner, J. W. Growth and characterization of graphite single crystals. *Carbon* **5**, 549-557, doi:10.1016/0008-6223(67)90032-2 (1967).

9 Derbyshire, F. J., Presland, A. E. B. & Trimm, D. L. Graphite formation by the dissolution - precipitation of carbon in cobalt, nickel and iron. *Carbon* **13**, 111-113, doi:10.1016/0008-6223(75)90267-5 (1975).

10 Konno, T. J. & Sinclair, R. Crystallization of amorphous carbon in carbon—cobalt layered thin films. *Acta Metallurgica et Materialia* **43**, 471-484, doi:10.1016/0956-7151(94)00289-t (1995).

11 Wang, Z., Jeurgens, L. P. H. & Mittemeijer, E. J. *Metal-Induced Crystallization: Fundamentals and Applications*. (Pan Stanford Publishing, 2015).

12 Anton, R. On the reaction kinetics of Ni with amorphous carbon. *Carbon* **46**, 656-662, doi:10.1016/j.carbon.2008.01.021 (2008).

13 Wenisch, R. *et al.* Nickel-enhanced graphitic ordering of carbon ad-atoms during physical vapor deposition. *Carbon* **100**, 656-663, doi:10.1016/j.carbon.2015.12.085 (2016).

14 Weatherup, R. S. *et al.* Introducing carbon diffusion barriers for uniform, high-quality graphene growth from solid sources. *Nano Lett* **13**, 4624-4631, doi:10.1021/nl401601x (2013).

15 Nakajima, Y. *et al.* Metal Catalysts for Layer-Exchange Growth of Multilayer Graphene. *ACS Appl Mater Interfaces* **10**, 41664-41669, doi:10.1021/acsami.8b14960 (2018).

16 Kelling, J., Zahn, P., Schuster, J. & Gemming, S. Elastic and piezoresistive properties of nickel carbides from first principles. *Physical Review B* **95**, doi:10.1103/Physrevb.95.024113 (2017).

17 Natesan, K. & Kassner, T. F. Thermodynamics of Carbon in Nickel, Iron-Nickel and Iron-Chromium-Nickel Alloys. *Metallurgical Transactions* **4**, 2557-2566, doi:10.1007/Bf02644258 (1973).

18 Sinclair, R., Itoh, T. & Chin, R. In situ TEM studies of metal-carbon reactions. *Microscopy and microanalysis : the official journal of Microscopy Society of America, Microbeam Analysis Society, Microscopical Society of Canada* **8**, 288-304, doi:10.1017/S1431927602020226 (2002).

19 Murata, H., Toko, K., Saitoh, N., Yoshizawa, N. & Suemasu, T. Direct synthesis of multilayer graphene on an insulator by Ni-induced layer exchange growth of amorphous carbon. *Applied Physics Letters* **110**, doi:10.1063/1.4974318 (2017).

20 Kim, K. J., Cho, S. Y., Kim, H. M. & Kim, K. B. Direct formation of graphene on dielectric substrate: Controlling the location of graphene formation adopting carbon diffusion barrier. *J Vac Sci Technol B* **36**, 021802, doi:10.1116/1.5016591 (2018).

21 Romanyuk, O. *et al.* Study of Ni-Catalyzed Graphitization Process of Diamond by in Situ X-ray Photoelectron Spectroscopy. *J Phys Chem C Nanomater Interfaces* **122**, 6629-6636, doi:10.1021/acs.jpcc.7b12334 (2018).

22 Saenger, K. L. *et al.* In situ x-ray diffraction study of graphitic carbon formed during heating and cooling of amorphous-C/Ni bilayers. *Applied Physics Letters* **96**, doi:10.1063/1.3397985 (2010).

23 Janke, D. *et al.* Influence of Nickel Catalyst Morphology on Layer-Exchange-Based Carbon Crystallisation of Ni/a-C Bilayers. *Phys Status Solidi B* **254**, doi:10.1002/pssb.201700234 (2017).

24 Bianco, A. *et al.* All in the graphene family - A recommended nomenclature for two-dimensional carbon materials. *Carbon* **65**, 1-6, doi:10.1016/j.carbon.2013.08.038 (2013).

25 Kouznetsov, V., Macák, K., Schneider, J. M., Helmersson, U. & Petrov, I. A novel pulsed magnetron sputter technique utilizing very high target power densities. *Surface and Coatings Technology* **122**, 290-293, doi:10.1016/s0257-8972(99)00292-3 (1999).

26 HZDR. *Equipment Nanocomposite Materials Group*, <https://www.hzdr.de/db/Cms?pNid=545> (2019).

27 Wenisch, R. *et al.* Cluster Tool for In Situ Processing and Comprehensive Characterization of Thin Films at High Temperatures. *Anal Chem*, doi:10.1021/acs.analchem.8b00923 (2018).

28 Mayer, M. in *AIP Conference Proceedings* 541-544 (1999).

29 Barradas, N. P., Jeynes, C. & Webb, R. P. Simulated annealing analysis of Rutherford backscattering data. *Applied Physics Letters* **71**, 291-293, doi:10.1063/1.119524 (1997).

30 Ferrari, A. C. Raman spectroscopy of graphene and graphite: Disorder, electron–phonon coupling, doping and nonadiabatic effects. *Solid State Communications* **143**, 47-57, doi:10.1016/j.ssc.2007.03.052 (2007).

31 Bravman, J. C. & Sinclair, R. The Preparation of Cross-Section Specimens for Transmission Electron-Microscopy. *J Electron Micr Tech* **1**, 53-61, doi:10.1002/jemt.1060010106 (1984).

32 Ferrari, A. C. & Robertson, J. Interpretation of Raman spectra of disordered and amorphous carbon. *Physical Review B* **61**, 14095-14107, doi:10.1103/PhysRevB.61.14095 (2000).

33 Abrasonis, G. *et al.* Sixfold ring clustering in sp(2)-dominated carbon and carbon nitride thin films: A Raman spectroscopy study. *Physical Review B* **73**, 125427, doi:10.1103/PhysRevB.73.125427 (2006).

34 Ferrari, A. C. *et al.* Raman spectrum of graphene and graphene layers. *Physical Review Letters* **97**, doi:10.1103/PhysRevLett.97.187401 (2006).

35 Ferrari, A. C. & Basko, D. M. Raman spectroscopy as a versatile tool for studying the properties of graphene. *Nature Nanotechnology* **8**, 235-246, doi:10.1038/nnano.2013.46 (2013).

36 Berciaud, S., Ryu, S., Brus, L. E. & Heinz, T. F. Probing the Intrinsic Properties of Exfoliated Graphene: Raman Spectroscopy of Free-Standing Monolayers. *Nano Letters* **9**, 346-352, doi:10.1021/nl8031444 (2009).

37 Malard, L. M., Pimenta, M. A., Dresselhaus, G. & Dresselhaus, M. S. Raman spectroscopy in graphene. *Phys Rep* **473**, 51-87, doi:10.1016/j.physrep.2009.02.003 (2009).

38 Lenski, D. R. & Fuhrer, M. S. Raman and optical characterization of multilayer turbostratic graphene grown via chemical vapor deposition. *Journal of Applied Physics* **110**, 013720, doi:10.1063/1.3605545 (2011).

39 Niilisk, A., Kozlova, J., Alles, H., Aarik, J. & Sammelselg, V. Raman characterization of stacking in multi-layer graphene grown on Ni. *Carbon* **98**, 658-665, doi:10.1016/j.carbon.2015.11.050 (2016).

40 Marchand, A., Lespade, P. & Couzi, M. *Characterization of carbon-carbon composites by Raman microprobe.* (1981).

41 Pimenta, M. A. *et al.* Studying disorder in graphite-based systems by Raman spectroscopy. *Physical chemistry chemical physics : PCCP* **9**, 1276-1291, doi:10.1039/b613962k (2007).

42 Ni, Z., Wang, Y., Yu, T. & Shen, Z. Raman spectroscopy and imaging of graphene. *Nano Research* **1**, 273-291, doi:10.1007/s12274-008-8036-1 (2008).

43 Reich, S. & Thomsen, C. Raman spectroscopy of graphite. *Philosophical Transactions of the Royal Society a-Mathematical Physical and Engineering Sciences* **362**, 2271-2288, doi:10.1098/rsta.2004.1454 (2004).

44 Tuinstra, F. & Koenig, J. L. Raman Spectrum of Graphite. *The Journal of Chemical Physics* **53**, 1126-1130, doi:10.1063/1.1674108 (1970).

45 Knight, D. S. & White, W. B. Characterization of diamond films by Raman spectroscopy. *Journal of Materials Research* **4**, 385-393, doi:10.1557/JMR.1989.0385 (1989).

46 Trucano, P. & Chen, R. Structure of graphite by neutron diffraction. *Nature* **258**, 136-137, doi:10.1038/258136a0 (1975).

47 Scherrer, P. *Bestimmung der Größe und der inneren Struktur von Kolloidteilchen mittels Röntgenstrahlen* 1918 edn, 98-100 (1918).

48 Melkhanova, S. *et al.* Carbon : nickel nanocomposite templates - predefined stable catalysts for diameter-controlled growth of single-walled carbon nanotubes. *Nanoscale* **8**, 14888-14897, doi:10.1039/c5nr06972f (2016).

49 Ungar, T., Dragomir, I., Revesz, A. & Borbely, A. The contrast factors of dislocations in cubic crystals: the dislocation model of strain anisotropy in practice. *Journal of Applied Crystallography* **32**, 992-1002, doi:10.1107/S0021889899009334 (1999).

50 Warren, B. E. *X-ray Diffraction*. (Dover Publications, 1990).

51 Rafaja, D. *et al.* Magnetic response of (Cr,Al,Si)N nanocrystallites on the microstructure of Cr—Al—Si—N nanocomposites. *Zeitschrift für Kristallographie* **225**, 599-609, doi:10.1524/zkri.2010.1347 (2010).

52 Rafaja, D., Krbetschek, C., Borisova, D., Schreiber, G. & Klemm, V. In situ X-ray diffraction study of stacking fault formation in the near-surface region of transformation induced plasticity steels. *Thin Solid Films* **530**, 105-112, doi:10.1016/j.tsf.2012.07.067 (2013).

53 Rafaja, D., Krbetschek, C., Ullrich, C. & Martin, S. Stacking fault energy in austenitic steels determined by using in situ X-ray diffraction during bending. *Journal of Applied Crystallography* **47**, 936-947, doi:10.1107/s1600576714007109 (2014).

54 Bozorth, R. M., Mason, W. P. & McSkimin, H. J. Frequency Dependence of Elastic Constants and Losses in Nickel. *Bell System Technical Journal* **30**, 970-989, doi:10.1002/j.1538-7305.1951.tb04439.x (1951).

55 Noyan, I. C. & Cohen, J. B. *Residual Stress: Measurement by Diffraction and Interpretation*. (Springer New York, 2013).

56 Zwell, L., Fasiska, E. J., Nakada, Y. & Keh, A. S. Dilation of Nickel Lattice by Dissolved Carbon. *Transactions of the Metallurgical Society of Aime* **242**, 765-& (1968).

57 Sheng, J., Welzel, U. & Mittemeijer, E. J. Nonmonotonic crystallite-size dependence of the lattice parameter of nanocrystalline nickel. *Applied Physics Letters* **97**, 153109, doi:10.1063/1.3500827 (2010).

58 Radic, N., Dubcek, P., Bernstorff, S., Djerdj, I. & Tonejc, A. M. Structural study of nanocrystalline nickel thin films. *Journal of Applied Crystallography* **40**, 377-382, doi:10.1107/S0021889807004682 (2007).

59 Martin, S., Ullrich, C., Simek, D., Martin, U. & Rafaja, D. Stacking fault model of epsilon-martensite and its DIFFaX implementation. *Journal of Applied Crystallography* **44**, 779-787, doi:10.1107/S0021889811019558 (2011).

60 Hemenger, P. & Weik, H. *On the existence of hexagonal nickel*. Vol. 19 (1965).

61 Wright, J. G. & Goddard, J. The lattice constants and magnetic anisotropy constants of electrodeposited single crystal films of hexagonal close-packed nickel. *Philosophical Magazine* **11**, 485-493, doi:10.1080/14786436508224236 (1965).

62 Kollie, T. G. Measurement of the thermal-expansion coefficient of nickel from 300 to 1000 K and determination of the power-law constants near the Curie temperature. *Physical Review B* **16**, 4872-4881, doi:10.1103/PhysRevB.16.4872 (1977).

63 Nelson, J. B. & Riley, D. P. The thermal expansion of graphite from 15 c. to 800 c.: part I. Experimental. *Proceedings of the Physical Society* **57**, 477-486, doi:10.1088/0959-5309/57/6/303 (1945).

64 Wazzan, A. R. Lattice and grain boundary self□diffusion in nickel. *Journal of Applied Physics* **36**, 3596-3599, doi:10.1063/1.1703047 (1965).

65 Siegel, D. J. & Hamilton, J. C. Computational study of carbon segregation and diffusion within a nickel grain boundary. *Acta Materialia* **53**, 87-96, doi:10.1016/j.actamat.2004.09.006 (2005).

66 Fitzer, E. & Kegel, B. Reaktionen von Kohlenstoffgesättigter Vanadiumcarbidschmelze mit ungeordnetem Kohlenstoff (Beitrag zur katalytischen Graphitierung). *Carbon* **6**, 433-446, doi:10.1016/0008-6223(68)90084-5 (1968).

67 Van Swygenhoven, H., Farkas, D. & Caro, A. Grain-boundary structures in polycrystalline metals at the nanoscale. *Physical Review B* **62**, 831-838, doi:10.1103/PhysRevB.62.831 (2000).

68 Mendelev, M. I., Zhang, H. & Srolovitz, D. J. Grain boundary self-diffusion in Ni: Effect of boundary inclination. *Journal of Materials Research* **20**, 1146-1153, doi:10.1557/JMR.2005.0177 (2005).

69 Dahlgren, S. D. *et al.* Microstructural Analysis and Tensile Properties of Thick Copper and Nickel Sputter Deposits. *Thin Solid Films* **40**, 345-353, doi:10.1016/0040-6090(77)90136-5 (1977).

70 Wang, Z. M., Wang, J. Y., Jeurgens, L. P. H. & Mittemeijer, E. J. Thermodynamics and mechanism of metal-induced crystallization in immiscible alloy systems: Experiments and calculations on Al/a-Ge and Al/a-Si bilayers. *Physical Review B* **77**, doi:10.1103/Physrevb.77.045424 (2008).

71 Sommer, F., Singh, R. N. & Mittemeijer, E. J. Interface thermodynamics of nano-sized crystalline, amorphous and liquid metallic systems. *Journal of Alloys and Compounds* **467**, 142-153, doi:10.1016/j.jallcom.2007.11.106 (2009).

72 Boer, F. R. d., Mattens, W. C. M., Boom, R., Miedema, A. R. & Niessen, A. K. *Cohesion in metals*. (North-Holland, 1988).

73 Zebda, A., Sabbah, H., Ababou-Girard, S., Solal, F. & Godet, C. Surface energy and hybridization studies of amorphous carbon surfaces. *Applied Surface Science* **254**, 4980-4991, doi:10.1016/j.apsusc.2008.01.147 (2008).

74 Shatynski, S. R. The thermochemistry of transition metal carbides. *Oxidation of Metals* **13**, 105-118, doi:10.1007/bf00611975 (1979).

75 Abrahamson, J. The surface energies of graphite. *Carbon* **11**, 337-362, doi:10.1016/0008-6223(73)90075-4 (1973).

76 Shchipalov, Y. K. Surface energy of crystalline and vitreous silica. *Glass and Ceramics* **57**, 374-377, doi:10.1023/A:1010900903019 (2000).

77 Pretorius, R., Harris, J. M. & Nicolet, M. A. Reaction of thin metal films with SiO2 substrates. *Solid-State Electronics* **21**, 667-675, doi:10.1016/0038-1101(78)90335-0 (1978).

78 Baird, J. D. & Taylor, J. Reaction between silica and carbon and the activity of silica in slag solution. *Transactions of the Faraday Society* **54**, 526, doi:10.1039/tf9585400526 (1958).

79 Thron, A. M., Greene, P., Liu, K. & van Benthem, K. In-situ observation of equilibrium transitions in Ni films; agglomeration and impurity effects. *Ultramicroscopy* **137**, 55-65, doi:10.1016/j.ultramic.2013.11.004 (2014).

Directionality of metal-induced crystallization and layer exchange in amorphous carbon/nickel thin film stacks

Daniel Janke[a], Frans Munnik[a], Jaakko Julin[a], René Hübner[a], Jörg Grenzer[a], Christina Wüstefeld[b], Sibylle Gemming[a,c], David Rafaja[b], Matthias Krause[a*]

[a] Helmholtz-Zentrum Dresden – Rossendorf, Bautzner Landstraße 400, 01328 Dresden, Germany

[b] Institute of Materials Science, TU Bergakademie Freiberg, Gustav-Zeuner-Straße 5, 09599 Freiberg, Germany

[c] Institute of Physics, TU Chemnitz, Reichenhainer Straße 70, 09126 Chemnitz, Germany

---

Individual contributions of the authors

Daniel Janke:	methodology, investigation, data curation, formal analysis, writing—original draft preparation, writing—review and editing
Frans Munnik	investigation, data curation, formal analysis, writing—original draft preparation
Jaakko Julin	investigation, data curation, formal analysis, writing—original draft preparation,
René Hübner	investigation, data curation, formal analysis, writing—original draft preparation, writing—review and editing
Jörg Grenzer	methodology, investigation, software, formal analysis, writing—original draft preparation, writing—review and editing
Christina Wüstefeld	methodology, writing—original draft preparation, writing—review and editing
Sibylle Gemming	conceptualization, writing—original draft preparation, writing—review and editing, supervision, funding acquisition
David Rafaja	conceptualization, software, methodology, writing—original draft preparation, writing—review and editing, supervision
Matthias Krause	conceptualization, methodology, formal analysis, writing—original draft preparation, writing—review and editing, supervision, project administration

* Corresponding author. Tel.: +493512603578; e-mail: matthias.krause@hzdr.de

For research articles with several authors, a short paragraph specifying their individual contributions must be provided. The following statements should be used “conceptualization, X.X. and Y.Y.; methodology, X.X.; software, X.X.; validation, X.X., Y.Y. and Z.Z.; formal analysis, X.X.; investigation, X.X.; resources, X.X.; data curation, X.X.; writing—original draft preparation, X.X.; writing—review and editing, X.X.; visualization, X.X.; supervision, X.X.; project administration, X.X.; funding acquisition, Y.Y.”,

Declaration of interests

☒ The authors declare that they have no known competing financial interests or personal relationships that could have appeared to influence the work reported in this paper.

☐The authors declare the following financial interests/personal relationships which may be considered as potential competing interests: